

STUDY OF GAS TURBINE EXHAUST DIFFUSER FLOW AND PERFORMANCE CHARACTERISTICS AT OFF-DESIGN CONDITIONS

S. Hummel, M. Bauer and D. M. Vogt

University of Stuttgart, Institute of Thermal Turbomachinery and Machinery Laboratory,
Stuttgart, Germany,
simon.hummel@itsm.uni-stuttgart.de

ABSTRACT

An experimental and numerical study has been conducted to assess the effect of inflow conditions on the performance of a generic axial exhaust diffuser design. The inlet conditions differ in magnitude and distribution of Mach number, swirl angle and radial total pressure profile allowing the investigation of various diffuser loads. Results are presented for two off-design loading conditions, representing an over-load and a part-load operating point. Additionally, the impact of tip leakage flow is examined. The results show the prominent role of supporting struts on the diffuser performance characteristics. At off-design conditions, severe inlet swirl reduces pressure recovery due to large strut separations while at the same time the positive effect of an additional energizing leakage flow is weakened.

KEYWORDS

axial diffuser, performance characteristics, off-design

NOMENCLATURE

Latin symbols

AR	area ratio
b	chord length (m)
c	velocity (m s^{-1})
C_p	pressure recovery coefficient
l	length (m)
Ma	Mach number
\dot{m}	mass flow rate (kg s^{-1})
p	pressure (Pa)
r	radius (m)
Re	Reynolds number

Greek symbols

α	swirl angle ($^\circ$)
β	kinetic energy parameter
θ	opening half-angle ($^\circ$)
ν	hub-to-tip ratio

Subscripts

ax	axial velocity component
circ	circumferential velocity component
n	normalized
rad	radial velocity component
s	static
t	total
x	streamwise location

Superscripts

$\bar{}$	average
\sim	area-averaged
$\hat{}$	massflow-averaged

Abbreviations

DL	design-load
OL	over-load
OP	operating point
PL	part-load
TLR	tip leakage ratio

INTRODUCTION

Axial exhaust diffusers make a significant contribution to increase the efficiency of power-generating gas turbines by recovering the residual kinetic energy behind the last turbine stage. In addition to maximize the rise in static pressure the uniformity of the diffuser outlet flow is of particular interest. In combined cycle power plants, a heat recovery steam generator (HRSG) is located downstream of the diffuser and requires a uniform inlet flow in order to work efficiently. For a given static pressure at the diffuser outlet (usually fixed by the HRSG), the pressure recovery of the diffuser enhances the turbine pressure ratio, resulting in an increase in power output and efficiency of the whole cycle. The pressure recovery primarily depends on the geometrical shape of the diffuser, especially with respect to area ratio and length, and is affected by endwall and mixing losses as well as non-converted kinetic energy at the diffuser outlet.

Research on diffuser performance goes back over six decades. Kline et al. (1959), Reneau et al. (1967) and Sovran and Klomp (1967) are among the classical pieces of work, summarizing experimental performance data on pressure recovery and expected flow regimes of rectangular, conical and annular diffusers. However, these early studies did not consider effects of varying diffuser inflow conditions. In terms of increasing the flexibility of the operation of power plants, the design of diffusers is challenging due to variation of turbine outflow. The typical inflow characteristics affecting the diffuser performance are the radial distribution of total pressure and swirl as well as tip leakage flow of the last turbine stage blades. In combination with an adverse pressure gradient in diffusers, a highly complex flow field with smooth wall separation, flow recirculation behind a blunt hub end and separated flow at supporting struts in the flow path can occur. Through the decades, numerous experimental and numerical investigations were completed to study the effect of inflow conditions on the diffuser performance and flow pattern. McDonald et al. (1971) and Kumar and Kumar (1980) conducted experimental investigations to determine the influence of inlet swirl on conical and annular diffuser performance, respectively. The main conclusion of both authors was the enhancement of pressure recovery with the introduction of swirl, in which the improvement was larger for aggressive diffusers, which were separated for axial inlet flow. A typical exhaust diffuser of a heavy-duty gas turbine includes supporting struts in the annular flow path for which the incidence angle to the incoming flow increases at off-design operation. Several authors such as Vassiliev et al. (2003), Dossena et al. (2017) and Brown et al. (2020) investigated the interaction between inflow swirl and struts regarding the overall diffuser performance. The influence of the total pressure was examined by Hirschmann et al. (2012). Studies about the impact of tip leakage flow can be found in Fleige et al. (2002) and Volkmer et al. (2011).

In this work, both experimental and numerical examinations of a generic diffuser geometry at off-design conditions concerning Mach number, total pressure distribution and inlet swirl were performed. Two operating points under detailed investigation being representative for extreme over-load and part-load are presented and extend the operating range investigated by Bauer et al. (2020). Additionally to the effect of inflow characteristics, the impact of tip leakage flow of a shrouded and unshrouded last turbine stage were examined.

DIFFUSER GEOMETRY AND EXPERIMENTAL SETUP

The generic diffuser geometry under investigation (see Fig. 1, diffuser section) is designed based on the diffuser charts given by Sovran and Klomp (1967). It is a 1:13 scaled model of an axial diffuser, which is representative for current heavy duty gas turbine exhaust diffusers. The diffuser consists of an annular section (A), including a row of six symmetrical NACA 0015

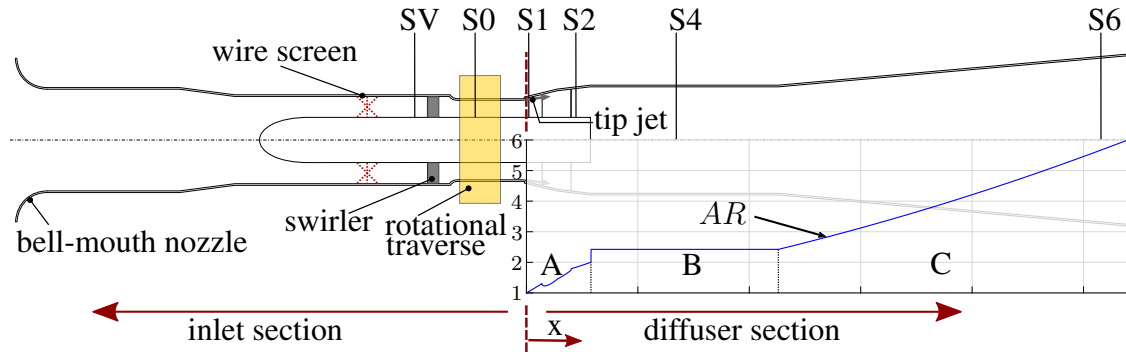


Figure 1: Sketch of the test rig with axial probe measurement plane distribution and area ratio of the diffuser section

struts, followed by a cylindrical (B) and a conical diffuser (C). The annular part features an opening half-angle of $\theta = 15^\circ$ at the inlet, reduced to $\theta = 7^\circ$ in the struts region. The inlet hub-to-tip ratio is $\nu = 0.55$. The straight hub has a diameter of 142.7 mm and ends abruptly at the end of the annular section. Downstream, the area ratio (AR) extends to 1.21 at the step diffuser and widens further downstream by an opening half-angle of $\theta = 5^\circ$ in the conical section to the diffuser outlet.

In addition to the diffuser itself, the test rig (see Fig. 1) offers an inlet section that is used to generate turbine related inflow conditions. At the test rig inlet, the main massflow is measured by means of a calibrated bellmouth nozzle with an accuracy of $\pm 1\%$. Afterwards, the total pressure profile is deflected by means of a wire-screen. All installed screens have a porosity of 58% with a wire thickness of 0.5 mm. A typical turbine outflow swirl (α) is induced by means of a stationary blade row. In addition, an axial tip flow that can be added at varying strength right at the diffuser inlet. Thereby, the tip leakage ratio (TLR) expresses the relative amount of added tip massflow with respect to the main massflow. The measurement error for the tip massflow has been determined to $\pm 1\%$. At the outlet the diffuser is connected to a model of a HRSG. The whole test rig is operated in suction mode.

For experimental investigations, the test rig features several axial and circumferential distributed static pressure taps at the endwalls and struts. The measurement error for the used pressure transducer is below ± 17 Pa. In addition, several locations for radial traverses of pneumatic five-hole cone probes are available along the test rig. Beside the radial traverse positions, a circumferential traverse is installed at the inlet plane S0, allowing circumferentially resolved measurements downstream of the swirler. The measurement error for the pressure transducer used for probe measurements is below ± 34 Pa. The probe head diameter for all pneumatic probes is 3 mm. In Fig. 1 and Fig. 2, the instrumentation scheme is shown.

For data evaluation, the recommendations according to Cumpsty and Hor-

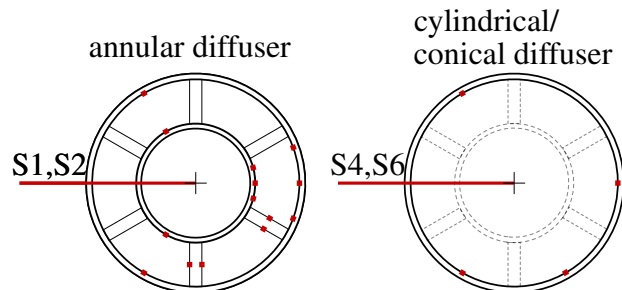


Figure 2: Instrumentation scheme for the annular, cylindrical and conical diffuser looking in the direction of flow; red squares mark the wall pressure locations, red lines symbolize the circumferential probe locations

lock (2006) are used, suggesting a massflow-averaged total pressure and an area-averaged static pressure. All data are reduced to ISO standard conditions. To ensure repeatability, all presented measurement data have been performed at least twice on different days and showed a deviation of the pressure recovery of $\Delta C_p < 0.8\%$ based on the casing pressure taps. Further details regarding the geometrical as well as the experimental setup can be found in Mihailowitsch et al. (2019) and Bauer et al. (2020).

Performance characteristics

The diffuser performance is quantified by means of the pressure recovery coefficient C_p . For this purpose, the averaged static wall pressure at the hub and casing and the massflow-averaged total pressure of the inlet traverse in plane S0 are used.

$$C_p = \frac{\bar{P}_{s,x} - \bar{P}_{s,S0}}{\hat{P}_{t,S0} - \bar{P}_{s,S0}} \quad (1)$$

To evaluate the non-uniformity of the flow, the kinetic energy parameter β in S6 is calculated, which is defined as the ratio of the actual massflow-averaged kinetic energy to the minimum kinetic energy of an ideal flow with an one-dimensional velocity profile and the same flow rate.

$$\beta = \frac{\frac{1}{\dot{m}} \int_A 1/2 \rho c^2 d\dot{m}}{1/2 \rho \tilde{c}_{ax}^2} = \underbrace{\frac{\frac{1}{\dot{m}} \int_A 1/2 \rho c_{ax}^2 d\dot{m}}{1/2 \rho \tilde{c}_{ax}^2}}_{\beta_{ax}} + \underbrace{\frac{\frac{1}{\dot{m}} \int_A 1/2 \rho c_{rad}^2 d\dot{m}}{1/2 \rho \tilde{c}_{ax}^2}}_{\beta_{rad}} + \underbrace{\frac{\frac{1}{\dot{m}} \int_A 1/2 \rho c_{circ}^2 d\dot{m}}{1/2 \rho \tilde{c}_{ax}^2}}_{\beta_{circ}} \quad (2)$$

Equation 2 shows that, with a minimum of unity, a more non-uniform and non-axial velocity across the flow area will increase β .

In this paper, all dimensions are normalized by the hub radius in S0 or to the strut chord length.

NUMERICAL MODEL

Three-dimensional steady and unsteady CFD simulations were performed using the commercial solver ANSYS CFX 18.2 to provide a more detailed insight into the flow behavior for further investigations and validation. The $k-\omega$ -SST turbulence model with reattachment modification by Menter (1994) is applied to close the (U)RANS equations given its well known suitability in flows with adverse pressure gradients.

The computational model of a 60° sector model shown in Fig. 3 consists of the swirler and the diffuser domain connected by means of a frozen rotor interface. Apart from a 60° sector model with periodic boundaries, computations are carried out for a full annulus model, as especially at off-design conditions, differences in the flow field prediction can occur (see Schäfer (2016)). The number of swirler blades depends on the operating point and is chosen in a way such as to obtain a pitch ratio of unity. The outlet of the conical diffuser part is extended axially with a cylindrical plenum to avoid flow reversal at the outlet boundary.

At the inlet of the swirler model, the measured radial total pressure distribution in SV with a total temperature of 288.15 K is set. The inlet turbulence intensity is defined with a constant value of 5% across the plane and the viscosity ratio is set to 10. At the diffuser outlet, the measured inlet massflow plus the additional tip jet massflow is defined. As an inlet boundary condition of the tip jet cavity, the measured massflow with a total temperature of 288.15 K is used.

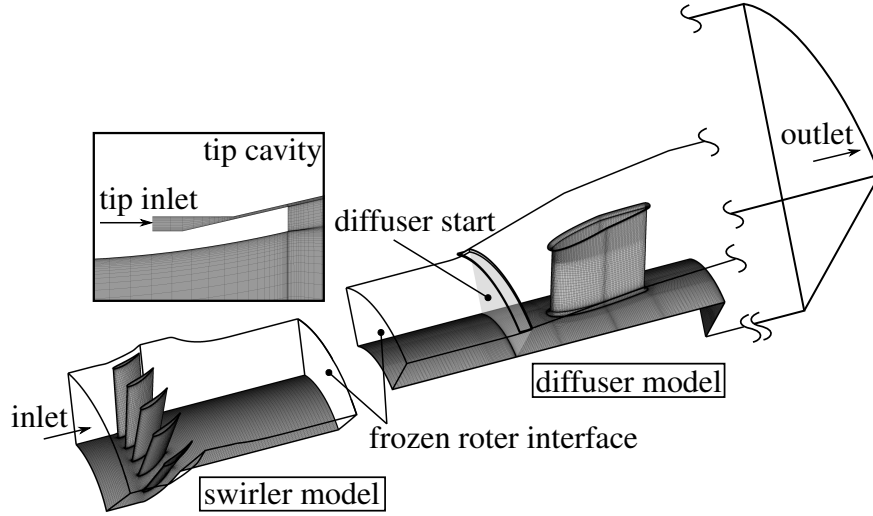


Figure 3: Computational model of the 60° sector model

The swirler grid was generated using Numeca Autogrid with a structured O4H mesh topology. The meshing of the diffuser was carried out using ANSYS ICEM CFD with structured hexahedral elements. To achieve a good resolution of the boundary layer, the averaged dimensionless wall distance is $y^+ < 1$. Based on a grid convergence study following the methodology outlined in Celik et al. (2008), the medium mesh for the sector model of over-load for example is composed of $6.12 \cdot 10^6$ cells. Results of different mesh sizes for the swirler and diffuser model are shown in Fig. 4. The averaged grid convergence index (GCI) between the coarse and medium mesh is $GCI_{\text{swirler}} = 0.3\%$ in the swirler S0 plane and $GCI_{\text{diffuser}} = 1.4\%$ for the casing values of the diffuser model. For the unsteady simulations of the sector model, a time step independence study was performed resulting in a physical time step of $\Delta t = 10^{-4}$ s. All unsteady results are time averaged with a time averaging interval of at least one diffuser throughflow.

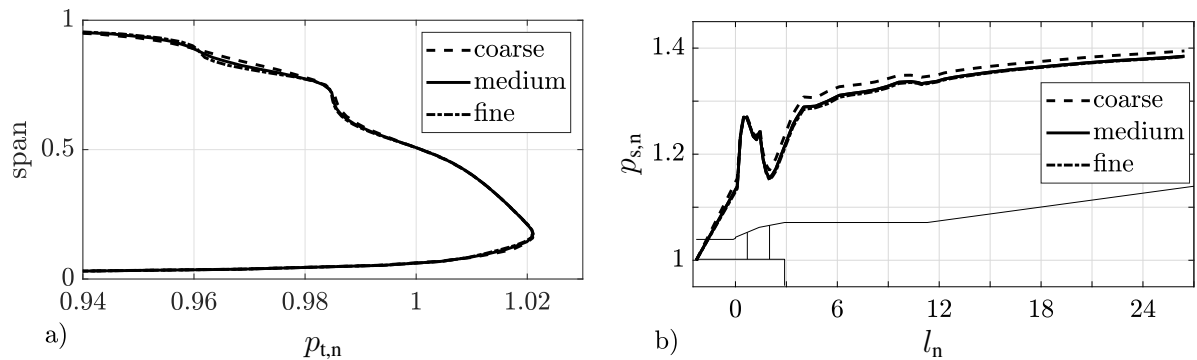


Figure 4: Grid independence study: a) normalized circumferentially averaged total pressure in S0 of the swirler model and b) normalized pressure distribution along the casing of the diffuser model for different mesh sizes according to Celik et al. (2008)

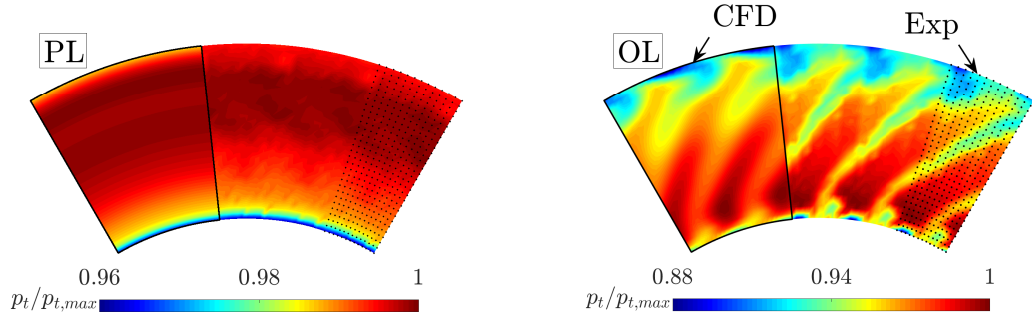


Figure 5: Total pressure distribution from the numerical model and from probe traverse measurements in plane S0 normalized by the maximum value; the points indicate the measuring location, the black edge indicates the numerical values

INFLOW CHARACTERISTICS

A detailed investigation of two off-design operating points (OP) is given in this work representing over-load (OL) and part-load (PL) conditions. The inflow characteristics in terms of total pressure, swirl angle and Mach number distribution are shown in Fig. 5 and Fig. 6 b), c), respectively, evaluated with radial traverse measurements for one swirler blade pitch. The numerical values are calculated at the identical radial and circumferential positions. The total pressure profiles of plane SV, which are generated through varying the wire-screen inclination and used as numerical inlet boundary conditions, are depicted in Fig. 6 a). Both off-design conditions extend the operating range investigated in Bauer et al. (2020). At OL, the total pressure increases towards the hub and the swirling flow is directed counterclockwise, whereas at PL, the inflow shows an increase of the total pressure from the hub to the casing with a clockwise swirl. The radial distribution of the circumferentially averaged inflow characteristics in plane S0 shows a good agreement between experiment and CFD. Local differences can be detected in Fig. 5. The swirler wakes are more pronounced in the experiment due to a comparatively higher surface roughness of the blading. Further deviations are visible in the endwall regions caused

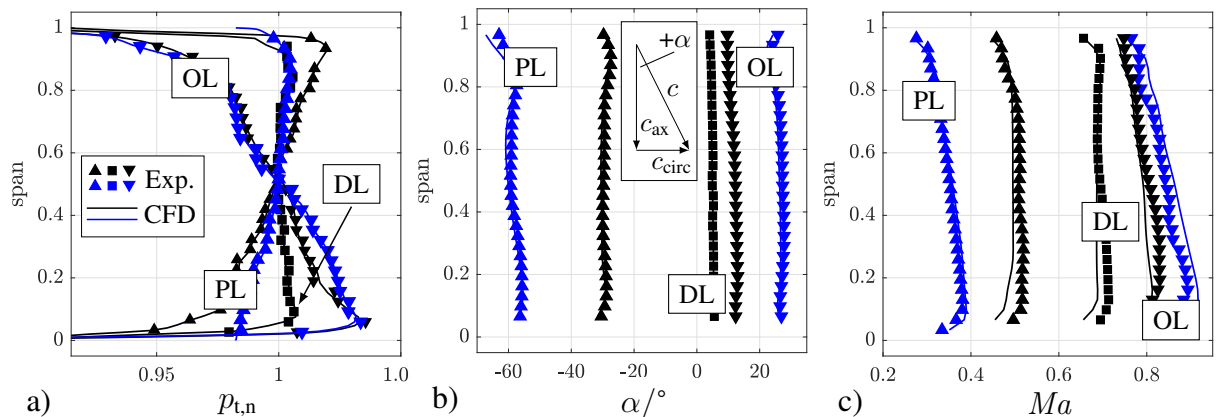


Figure 6: Radial distribution of a) total pressure normalized to its p_t at 50% span in SV and circumferentially averaged b) swirl angle and c) Mach number in S0; blue profiles show the inlet conditions in this study, black profiles represent the examined design and off-design conditions in Bauer et al. (2020)

by probe-wall interactions and a different prediction of secondary flows. Considering the whole evaluation plane, computed and measured total pressure distribution are in good agreement.

The Reynolds number calculated with the hydraulic diameter in S0 is in the range of $Re = 0.67 \cdot 10^6 - 1.2 \cdot 10^6$ depending on the OP. Each OP is investigated without (TLR00) as well as with an energizing tip leakage flow of 2% (TLR20) of the respective OP main mass flow.

RESULTS AND DISCUSSION

In this section the diffuser performance and the flow field at extreme OL and PL condition are discussed and the influence of energizing tip leakage flow is depicted. The description and evaluation of the operating points is based on the pressure recovery distribution along the casing and struts. At each axial location, the circumferential distributed pressure taps are averaged arithmetically. In addition, radial traverse data of total pressure (normalized to the measured massflow-averaged total pressure in S0) are shown which are located in the middle of a strut passage along the diffuser. It should be noted that a lack of measured traverse data indicates very low velocities outside the probe calibration range ($Ma < 0.05$) or flow recirculation zones. Furthermore, the numerical results are based on the full annulus model except in the figures of pressure recovery along the diffuser length, where different modeling approaches are shown. Finally, a comparison of design to off-design conditions regarding pressure recovery and non-uniformity of the diffuser outflow based on the kinetic energy parameter β is made, including the operating points investigated by Bauer et al. (2020).

Over-Load

The over-load condition is characterized by an hub-strong radial total pressure distribution, a midspan swirl angle of $\alpha = 25^\circ$ and an averaged Mach number of $Ma = 0.85$ (see Fig. 6).

The high inlet swirl comes along with an incidence-induced strut separation resulting in high losses and a reduced local pressure recovery. This can be seen in Fig. 8 with a decreasing C_p at a diffuser length $l_n = 1.43$ for both tip leakage cases. Without tip leakage flow, the flow separates at the casing right at the diffuser inlet with a reattachment that is predicted before the

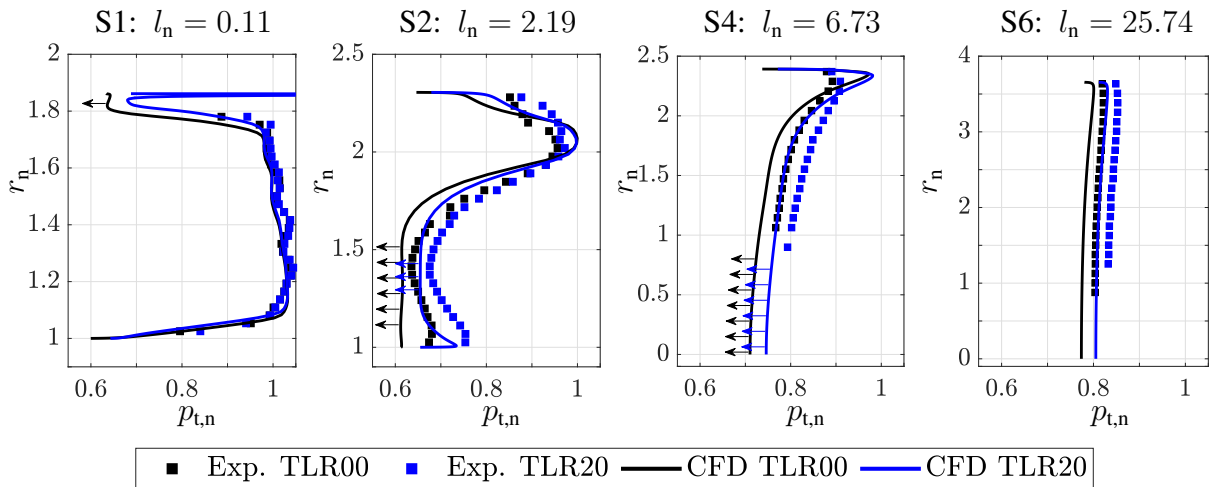


Figure 7: Radial distribution of normalized total pressure in different traverse planes along the diffuser length at OL; arrows indicate computed separation region with $c_{ax} < 0 \text{ m s}^{-1}$

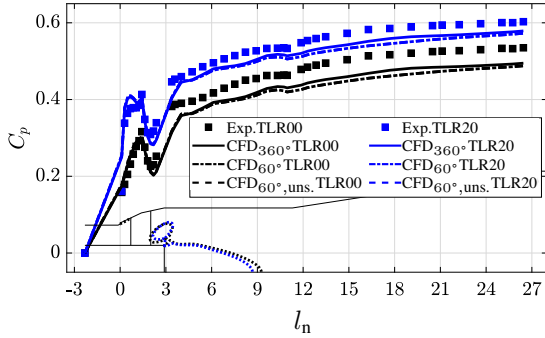


Figure 8: Pressure recovery along the casing and computed separation zones at OL

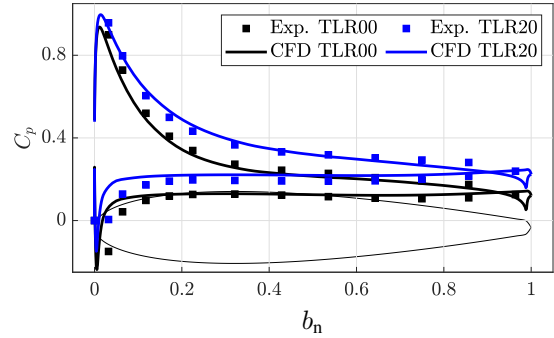


Figure 9: Pressure recovery along the strut at 50% of the channel height at OL

strut leading edge. Figure 14 shows a visual representation of the computed separation zones in the annular diffuser to clarify the flow separation behavior. The onset of the strut separation at midspan is close to the leading edge (see Fig. 9) and is numerically predicted over the entire span. Contrary to the experiment, the computed S2 traverse values (see Fig. 7) depict an area of recirculation for $1.12 < r_n < 1.51$. Therefore the circumferential extension in CFD is more pronounced and the pressure recovery is predicted to be smaller downstream of the trailing edge. Furthermore, the lower pressure recovery downstream of the blunt hub end in Fig. 8 indicates a delayed closure of the computed strut separation. The analysis of the 3D CFD flow field indicates, that an increased swirl near the hub results in a more pronounced circumferential extension of the strut separation in this area. This leads to a severe flow acceleration in the unblocked area and a casing-strong total pressure distribution from S2 to S6. As a result of the overestimated computed strut separation compared to the experiment, the losses are higher and the total pressure level is lower in S4 and S6.

By adding tip leakage flow and energizing the boundary layer, the casing separation is suppressed. The influence of the tip leakage flow is mainly limited by the flow field in the annular diffuser. However, the inflow condition in S1 remains unaffected with the exception of the casing region, where the high momentum of the tip leakage flow can be observed. The increase in pressure recovery at the diffuser outlet (see Fig. 8) compared to the case without tip leakage flow is primarily introduced by the suppressed casing separation. The flow deceleration upstream of the strut is therefore stronger, resulting in a larger swirl angle. Despite the increase of the computed averaged swirl by approximately 1.5° upstream of the strut, the strut loading at midspan is nearly unaltered, but features a higher pressure level (see Fig. 9). With additional tip leakage flow, the shape of the strut separation has changed slightly and the computed separation still exceeds the middle of the strut passage in plane S2 (see Fig. 7). Further downstream in the cylindrical diffuser, experiment and CFD show the same trend of a shortened hub wake (see Fig. 7, S4 and Fig. 8).

It is visible in Fig. 8, that the CFD results of the steady-state simulation (CFD_{60°) and the unsteady simulation ($CFD_{60^\circ,uns.}$) show no differences and therefore it is not necessary to apply the investigated URANS modeling. Larger differences exist for the full annulus model (CFD_{360°) which shows a better agreement of pressure recovery to the experiment, particularly downstream of the hub end.

Part-Load

At part-load, the inlet profile features a tip-strong total pressure distribution at a midspan swirl angle of $\alpha = -60^\circ$ and an averaged Mach number of $Ma = 0.3$ (see Fig. 6).

The severe circumferential velocity of the swirling flow forces high energy of the main flow towards the casing, where the momentum exchange with the boundary layer is increased. As a consequence, the boundary layer on the hub is weakened to such an extent that the flow separates upstream of the diffuser start $l_n = 0$. Figure 10 shows the radial distribution of the normalized circumferential velocity $c_{\text{circ},n} = c_{\text{circ}}/\tilde{c}_{\text{circ},S0}$ with the circumferential velocity c_{circ} and the area-averaged circumferential velocity $\tilde{c}_{\text{circ},S0}$ in plane S0. The radial position r_n extends from the hub up to the middle of the channel. The computed velocity is higher which causes a greater radial extension of the hub separation in S1. This can be seen in the traverse data at S1 in Fig. 11. The smaller hub separation in the experiment results in a comparatively higher pressure recovery for $l_n < 1.05$. The adverse effect of the separated flow near the hub regarding the pressure recovery is shown in Fig. 12. Due to the high swirl magnitude, a strut separation occurs at midspan as expected (see Fig. 13). The onset of the large-scaled separation at the strut further reduces the pressure recovery up to a measured minimum of $C_p = -0.12$ at $l_n = 1.81$. The mismatch of the strut loading between experiment and CFD comes as a consequence of the overestimated computed hub separation. The separated flow on the hub reattaches downstream of the strut leading edge as the flow is further accelerated due to the blockage of the separation bubble on the strut. The boundary layer on the hub stays attached until the abrupt hub end. Missing measured traverse data and computed recirculation zones in S2 (see Fig. 11) illustrate the stronger distortion of the strut separation in circumferential direction compared to over-load. The increasing area ratio and closing strut separation come along with an enhanced pressure recovery at the transition between annular and cylindrical diffuser. Downstream of the blunt hub end, a recirculation zone establishes (see Fig. 12 and Fig. 11, S4).

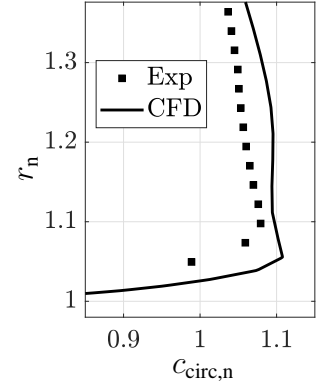


Figure 10: $c_{\text{circ},n}$ in S0 from hub up to the middle of the channel at PL

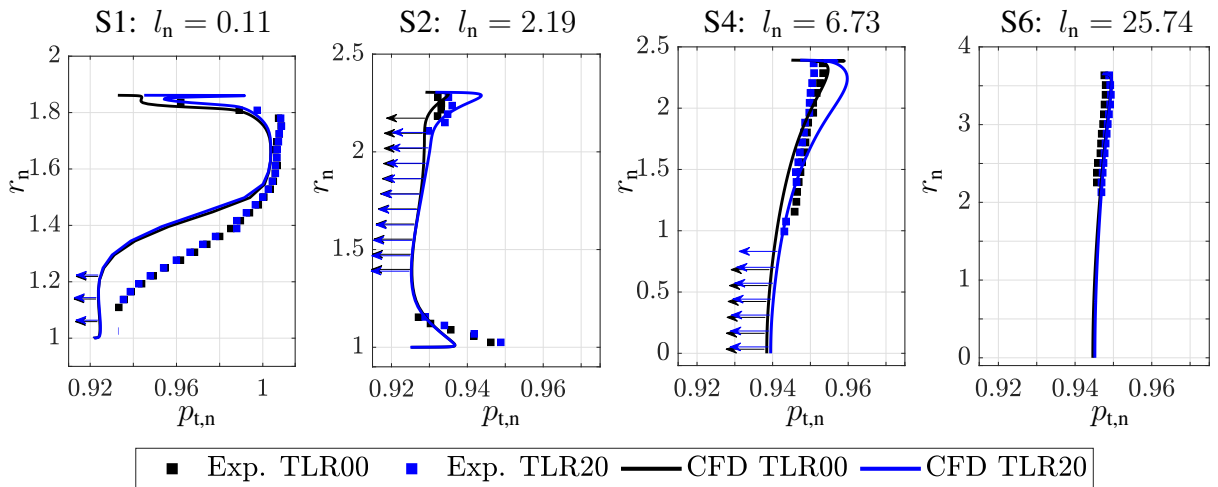


Figure 11: Radial distribution of normalized total pressure in different traverse planes along the diffuser length at PL; arrows indicate computed separation region with $c_{\text{ax}} < 0 \text{ m s}^{-1}$

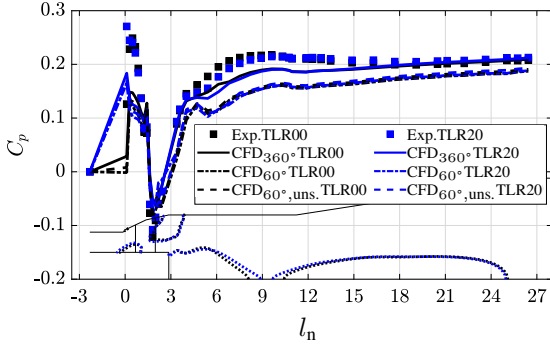


Figure 12: Pressure recovery along the casing and computed separation zones at PL

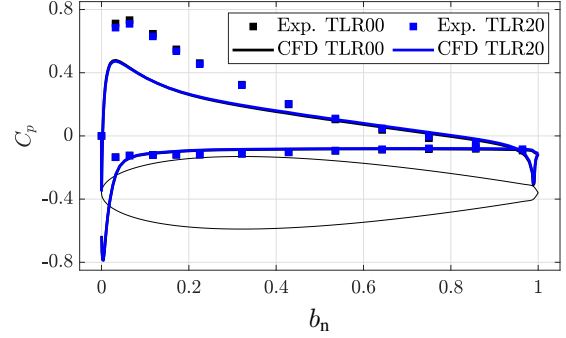


Figure 13: Pressure recovery along the strut at 50% of the channel height at PL

Initially, the zone closes in CFD before it reappears further downstream due to low energy fluid in the center area of the diffuser and an increasing casing radius in the conical diffuser. A similar trend can be observed in the experiment based on the distribution of C_p in Fig. 12. However, the recirculation zone in the cylindrical diffuser is smaller resulting in a higher pressure recovery. Furthermore, the measured maximum in pressure recovery along the diffuser is already reached in the cylindrical part at $l_n = 9.6$. In the conical diffuser, more pressure relative to its inlet is recovered in CFD giving hint of a different recirculation zone until the diffuser outlet.

Additional tip leakage flow has no significant influence on the diffuser performance and flow field due to the high inlet swirl. Minor variations occur in the hub wake region of the cylindrical diffuser though (see Fig. 11, S4 and Fig. 12).

The application of a full annulus model at extreme part-load is superior in terms of a better agreement to measured diffuser performance. Variations of the flow field within the annular diffuser passages are detectable for this model and the computed recirculation zone downstream of the hub shows a slight asymmetry.

Comparison of design to off-design conditions

Figure 14 summarizes the diffuser performance in terms of pressure recovery over the whole investigated operating range including the design and off-design conditions described in Bauer et al. (2020). The pressure recovery at the casing is evaluated at the last axial position of the three diffuser sections, respectively. The figure includes the experimental data in form of symbols and the corresponding deviation of the CFD values in form of bars. For a visual representation of the flow separation behavior the computed separation zones in the annular diffuser are shown for all cases.

In general, inlet swirl and additional tip leakage flow are strongly related to pressure recovery. Excessive swirl leads to extensive separation over the struts resulting in reduced pressure recovery. The increasing swirl at off-design reduces casing separation for the TLR00-cases, which is the reason why additional tip leakage is less effective there. The static pressure rise in the cylindrical diffuser is quite similar for all OP at TLR00. The conical diffuser shows a performance gain of approximately 15% compared to the C_p level at the cylindrical exit regardless of the inflow conditions at TLR00 as long as the boundary layer at the casing stays attached and no recirculation zone in the diffuser centerline exists. However, at extreme part-load operation, the conical section has nearly no potential to convert excess kinetic energy to static pressure rise. For this off-design condition, the diffuser showed the maximum measured drop of 74% in

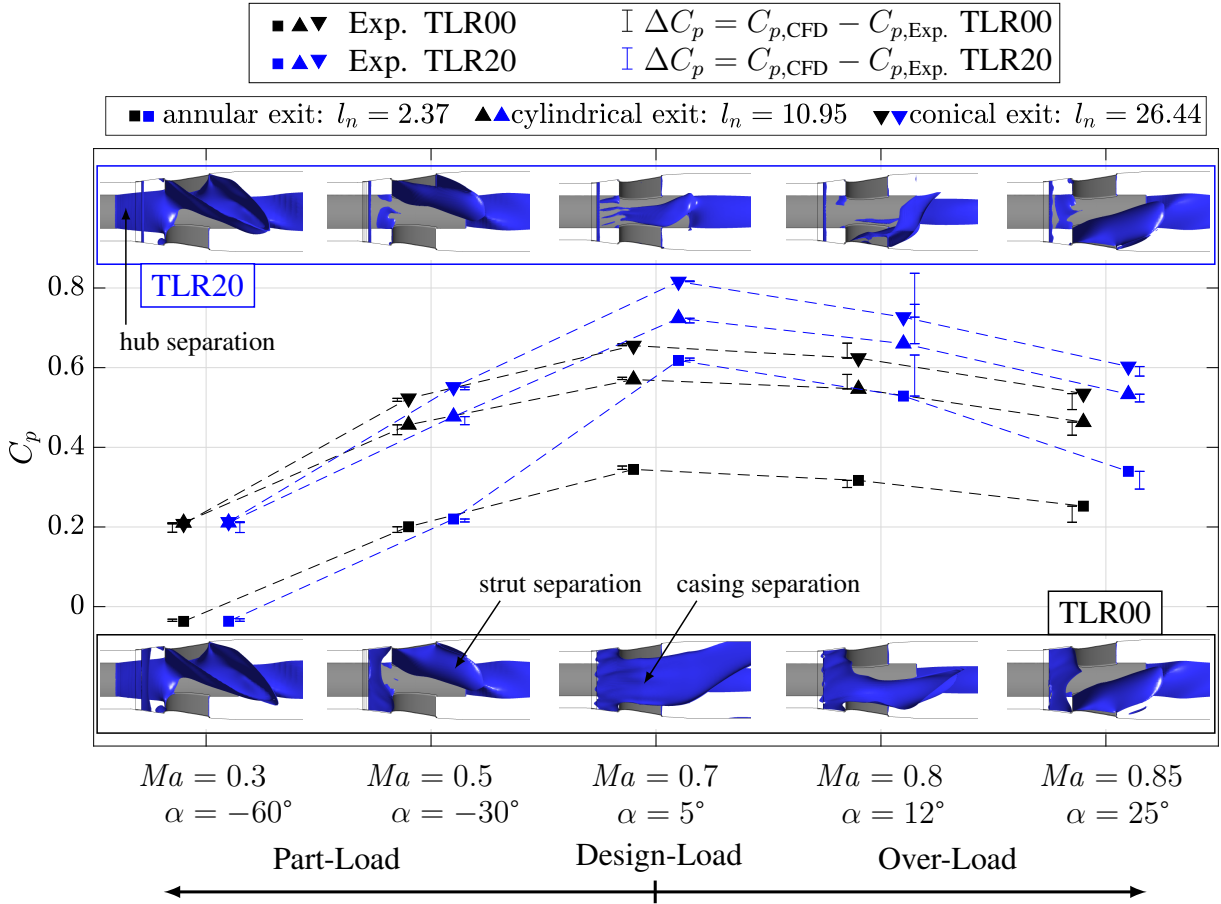


Figure 14: Pressure recovery coefficient of casing data at representing position of annular, cylindrical and conical diffuser exit of all operating points including design and off-design OP investigated by Bauer et al. (2020) for TLR00 and TLR20; bars show the deviation of the corresponding computed values; blue isosurfaces $c_{ax} = 0 \text{ m s}^{-1}$ indicate computed separations

C_p at the conical outlet relative to design-load with tip leakage flow. In the case of TLR20, the performance of the different diffuser sections are highly dependent on the operating point. At design-load for example, the major part of the pressure recovery occurs in the annular diffuser, whereas at PL, $\alpha = -30^\circ$, the cylindrical part shows the strongest increase of pressure recovery.

The computed pressure recovery is underpredicted for all OP compared to the experiment due to a overprediction of strut and endwall separations with the exception of OL, $\alpha = 12^\circ$. At this OP, the inflow swirl is near the critical incidence angle of $\alpha \approx 17^\circ$ of the strut at which the flow separates. Larger separations occur in the measurement resulting in a 15% lower C_p at the diffuser outlet as opposed to the CFD.

Figure 15 shows the non-uniformity of the flow in the exit traverse S6 based on the kinetic energy parameter β . Experimental data of the complete radial traverse are not available at each OP due to low velocities near the diffuser centerline. For this reason, the computed velocity profile is also evaluated over the entire height. The measured traverse data show a more uniform and more axial velocity distribution for all OP compared to CFD. This can be attributed to the

deficiencies of the used turbulence model, where the shear stresses in the free shear layers are underpredicted. The radial component β_{rad} shows an extremely small percentage of the kinetic energy parameter over the whole operating range. At off-design, excess kinetic energy of the inflow due to high inlet swirl still exists at the diffuser outlet and is not converted to static pressure rise. With additional tip leakage flow, the exit flow becomes more axial at DL. The difference between β_{ax} at TLR00 and TLR20 is more pronounced for the computation. A clear trend at OL and PL can not be observed.

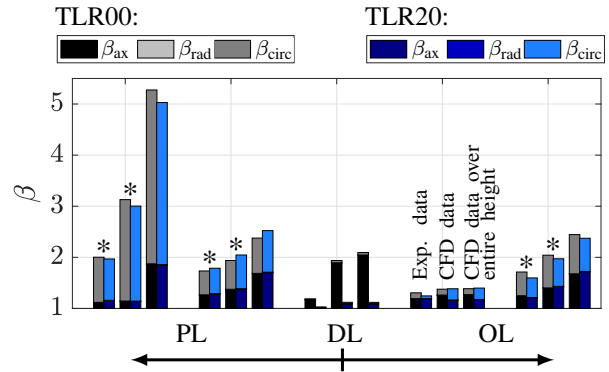


Figure 15: Kinetic energy parameter β in exit traverse S6;*) constrained radial evaluation

CONCLUSIONS

An experimental and numerical study on the performance characteristics of a generic axial exhaust diffuser at off-design conditions has been presented. The inflow conditions varies in terms of swirl angle, radial total pressure profile, Mach number and tip leakage flow, representing typical part-load and over-load operating points of an industrial gas turbine. The study shows that the diffuser performance is heavily affected by the flow around the diffuser struts. Due to high inlet swirl at off-design, incidence-induced separations from the leading edge of the struts result in a considerable reduction of pressure recovery. In such cases, the influence of tip leakage flow is less pronounced. However, increasing circumferential velocity at off-design enhances the risk of a hub separation and a recirculation zone in the center of the cylindrical and the conical diffuser section. In further investigations, strut design improvements or measures to reduce the high losses resulting from large-scaled strut separations can be considered.

The numerical prediction of strut and endwall separations with simultaneous superposition of adverse pressure gradient in axial direction is challenging for the underlying computational model. The differences between the CFD results applying the SST turbulence model with reattachment modification and the experimental data are attributed to an overprediction of strut and endwall separations resulting in underpredicting pressure recovery. To improve the quality of the numerical results, scale resolving models could be applied.

ACKNOWLEDGEMENTS

The authors would like to thank Siemens Energy for their support and their permission to publish the work. Part of the work presented in this paper is funded by the Bundesministerium für Wirtschaft und Energie within the cooperative research program AG TURBO, Verbundvorhaben ECOFlex-turbo, Teilvorhaben 4.2.2, FKZ03ET7091K. The responsibility for the content of the publication rests with the authors. Acknowledgement is also given to the staff of the ITSM and Ali Akturk from Siemens Energy for their invaluable support during this project.

REFERENCES

Bauer, M., Hummel, S., Schatz, M., Kegalj, M. and Vogt, D. M. (2020). *Investigation of the Flow Field and the Pressure Recovery in a Gas Turbine Exhaust Diffuser at Design, Part-load and Over-load Condition*, In Proceedings of ASME Turbo Expo 2020, GT2020-14310.

- Brown, K., Guillot, S., Ng, W., Iksang, L., Dongil, K. and Hong, G. (2020). *Experimental Investigation of Gas Turbine Axial Diffuser Performance: Part II – Effect of Inlet Flow Profiles at On- and Off-Design Conditions*, In Proceedings of ASME Turbo Expo 2020, GT2020-15305.
- Celik, I. B., Ghia, U., Roache, P. J., Freitas, C. J., Coleman, H. and Raad, P. E. (2008). *Procedure for Estimation and Reporting of Uncertainty Due to Discretization in CFD Applications*, ASME, J. Fluids Eng., 130(7): 078001 (9 pages).
- Cumpsty, N. A. and Horlock, J. H. (2006). *Averaging Nonuniform Flow for a Purpose*, ASME, J. Turbomach., 120(1): 120–129.
- Dossena, V., Persico, G., Paradiso, B., Bettini, C., Canelli, C., Cecchi, S. and Daccà, F. (2017). *Investigation of the Flow Field in a Gas Turbine Exhaust Diffuser at Design and Part Load Conditions*, In Proceedings of the 1st Global Power and Propulsion Forum, GPPF-2017-32.
- Fleige, H., Riess, W. and Seume, J. (2002). *Swirl and Tip Leakage Flow Interaction with Struts in Axial Diffusers*, In Proceedings of ASME Turbo Expo 2002, GT-2002-30491.
- Hirschmann, A., Volkmer, S., Schatz, M., Finzel, C., Casey, M. and Montgomery, M. (2012). *The Influence of the Total Pressure Profile on the Performance of Axial Gas Turbine Diffusers*, ASME, J. Turbomach., 134(2): 021017 (9 pages).
- Kline, S. J., Abbott, D. E. and Fox, R. W. (1959). *Optimum Design of Straight-Walled Diffusers*, ASME, J. Basic Eng., 81(3): 321–331.
- Kumar, D. S. and Kumar, K. L. (1980). *Effect of Swirl on Pressure Recovery in Annular Diffuser*, J. Mech. Eng. Science, 22(6): 305–313.
- McDonald, A. T., Fox, R. W. and Van Dewoestine, R. V. (1971). *Effects of Swirling Inlet Flow on Pressure Recovery in Conical Diffusers*, AIAA J., 9(10): 2014–2018.
- Menter, F. R. (1994). *Two-Equation Eddy-Viscosity Turbulence Models for Engineering Applications*, AIAA J., 32(8): 1598–1605.
- Mihailowitsch, M., Schatz, M. and Vogt, D. M. (2019). *Numerical Investigations of an Axial Exhaust Diffuser Coupling the Last Stage of a Generic Gas Turbine*, ASME, J. Eng. Gas Turbines Power, 141(3): 031025 (9 pages).
- Reneau, L. R., Johnston, J. P. and Kline, S. J. (1967). *Performance and Design of Straight, Two-Dimensional Diffusers*, ASME, J. Basic Eng., 89(1): 141–150.
- Schäfer, P. (2016). *Verbesserung des Druckrückgewinns in axialen Kraftwerksdiffusoren*, PhD thesis, Ruhr-University of Bochum.
- Sovran, G. and Klomp, E. D. (1967). *Experimentally Determined Optimum Geometries for Rectilinear Diffusers with Rectangular, Conical or Annular Cross-Section*, In G. Sovran (ed.), Fluid Mechanics of Internal Flow, Elsevier Publ. Comp., pp. 270–319.
- Vassiliev, V., Irmisch, S. and Claridge, M. (2003). *Experimental and Numerical Investigation of the Impact of Swirl on the Performance of Industrial Gas Turbines Exhaust Diffusers*, In Proceedings of ASME Turbo Expo 2003, GT2003-38424.
- Volkmer, S., Hirschmann, A., Casey, M. and Montgomery, M. (2011). *The Impact of a Tip Leakage Jet on Flow Separation in Axial Gas Turbine Diffusers*, In Proceedings of 9th European Conference on Turbomachinery, Fluid Dynamics and Thermodynamics.